Title: Micro-computed tomography of tubular braided composites
Authors: Garrett W. Melenka [a], Eric Lepp [a], Benjamin K. Cheung [a], Jason P. Carey [a*1]
Affiliations: [a] University of Alberta

Abstract: Two dimensional (2D) tubular braided composites consist of textile fibers imbedded in a resin matrix. Braid geometry and void content will affect the mechanical behavior of the tubular braided composite samples. In this study, tubular braid samples were assessed using micro X-ray computed tomography (μCT) to evaluate sample porosity/void content and to identify the strand geometry of the reinforcing fibers. The process described in this manuscript can be used to assess the quality and consistency of the tubular braided composite manufacturing process.

Keywords: Textile composites; x-ray tomography; Porosity/voids; braided composites

1 Introduction

Two dimensional (2D) tubular braided composites comprise of woven fibers impregnated within a resin matrix [1, 2]. Tubular braided composites (TBC's) are manufactured by weaving fibers onto a mandrel; the fibers are then saturated with resin to produce a final product [1]. Braiding allows for the angle between fibers to be varied whereas the angle of woven fibers is fixed [3]. The material properties of braided composites can be altered by varying the resin, fiber or braid geometry (fiber density or braid angle). This versatile manufacturing method could be applied to a range of engineering fields that include biomedical devices, sports equipment, automotive, or structural applications [4].

Similar to composite laminates, the mechanical properties of tubular braided composites can be predicted using the braid geometry and with the mechanical properties of the composite constituents [5, 6]. Accurate knowledge of the matrix and fiber volume fractions is required for these mechanical models. Currently, mechanical models for tubular braided composites assume an idealized geometry for predicting material properties. Accurate knowledge of tubular

[1] *Corresponding Author

composite tow architecture is also required to model the mechanical properties of tubular braided composites. Several methods have been used to model the geometry of composite braids. Composite braid geometries were initially modeled using the mosaic model of Ishikawa and Chou [7] and the fiber undulation model of Naik *et al* [8]. Recently, braid strand path has been modeled by assuming fibers follow a sinusoidal path [6, 9, 10]; however, these models do not account for variations that may occur during composite braid manufacturing. To assess the accuracy of these models, it is necessary to develop a technique is necessary to evaluate the accuracy and consistency of tubular braids manufactured using a Maypole braider.

Void volume fraction in tubular composite braids impact matrix volume fraction and strand macro-mechanics. Voids can adversely affect mechanical properties [11, 12]. The void content is conventionally determined using methods such as matrix digestion or matrix burn off [13]; these provide the total void content of the composite sample but do not provide information on the distribution or size of voids within the sample geometry. Void content can also be determined using optical microscopy analysis methods in order to quantify void content [14, 15]. Optical methods are time intensive as successive 2D cross-sections of the composite sample are required. Finally, optical microscopy, matrix burn off and matrix digestion are destructive methods [16, 17].

A method that allows for both the determination of fiber tow architecture and void content is x-ray micro-computed tomography (μCT) [18][15]. X-ray μCT creates a cross-sectional image of an object. Contrast seen in the scan images is the result of differences in x-ray attenuation. Material density and elemental composition both affect the attenuation of a sample, allowing for differentiation of different materials within a single μCT sample.

The complex fiber-tow-architecture of flat composite braids has been examined with μCT [19-21]. Void content for textile composites [22, 23] as well as void content measurement and fiber tow geometry has focused on flat textiles or 3D woven textiles [19, 20, 22, 23] have been investigated using standard methods. Little and Schilling [24, 25] performed void content measurement of composite laminates using μCT images, but these structures lack the complexity of the braided interwoven structure. To the best of the author's knowledge no works in the literature exist that investigate void content or fiber tow architecture for tubular braided composites using a μCT measurement method. As well, there is little literature which investigates the void content of tubular braided composites. Void content has been assessed for tubular braided composites using acid digestion and ultrasonic methods [26, 27] however neither of this methods provide information on the statistical distribution of voids throughout a composite sample [28].

The aim of this study is to investigate imperfections and voids of tubular braided composites using a μCT measurement method. The size and distribution of voids and imperfections throughout the tubular braid structure will be measured to assess the statistical distribution of defects in the braid structure. In addition, the tubular braid geometry will be investigated to quantify the individual yarn cross-sectional area, aspect ratio, braid angle and braid strand period. Accurate measurement is necessary to improve current braid geometrical models and to assess the quality and consistency of the braid manufacturing process. To simplify and automate the braid strand identification and measurement process, a cylinder unwrapping algorithm has been developed to convert the original tubular braid μCT images into a flattened braid structure.

This study will provide a new method for accurately assessing braid strand path geometry and voids content measurements that are necessary for accurate prediction of tubular composite braid material properties and modeling [5, 6].

2 Methods

The tubular braided preform was prepared using a Maypole braider (Steeger USA, K80-72, Steeger USA, Inman, SC). The braid preform was manufactured using Kevlar (Kevlar49, 5680 Denier, Dupont, Mississauga On) fibers. The braid was manufactured in a diamond braid configuration using 18 carriers. Once the braid perform was manufactured, it was placed over an 11.1mm (7/16") Tethlon (polytetrafluoroethylene (PTFE)) mandrel and impregnated with a thermoset resin (Epon825, Momentive Specialty Chemicals Inc., Columbus OH) and hardener (Ancamine1482, Air Products, Allentown PA) combination with a resin to hardener ratio of 100:19. The braid was then oven cured at 110°C for 2 hours. An example of a braid preform and cured braid sample are shown in Figure 1.

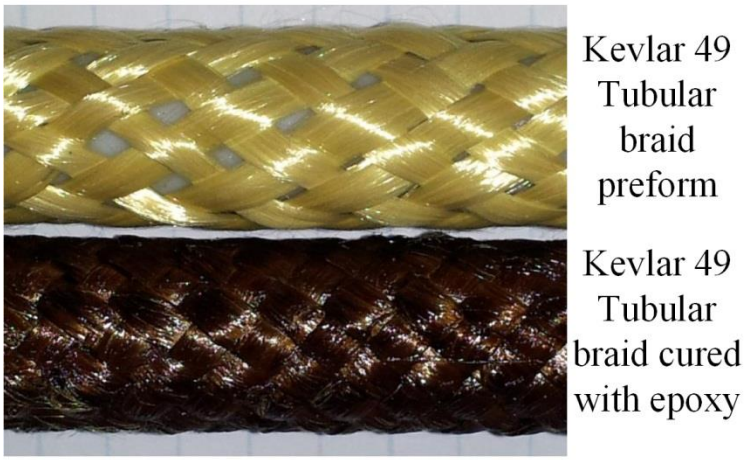

Figure 1: Tubular braided composites Top: Kevlar49 braid preform bottom: Cured Kevlar49 braid with an epoxy resin

Non-destructive μCT measurement technique was used to quantify voids within tubular braided composite structures and to assess the braid fiber strand geometry. Most μCT studies of composites have focused on glass and carbon fiber composites as opposed to Kevlar fibers [12, 19, 20, 22, 23]. The braid sample was imaged using a Skyscan 1076 μCT scanner (Bruker-MicroCT, Kontich, Belgium). The X-Ray beam energy used in this study was 51 kV at 110 μA. The μCT images collected in TIFF image format were 2000 x 1048 pixels with a voxel size of 18.2 μm^3 and a bit depth of 16. The μCT images were imported into NRecon v1.6.9 (SKYSCAN, Kontich, Belgium), to produce bitmap images containing cross-sectional slices of the scanned sample. The final bitmap images have an image size of 2000 x 2000 pixels. An example of the two-dimensional cross-sectional slice of the tubular braid sample is shown in Figure 2.

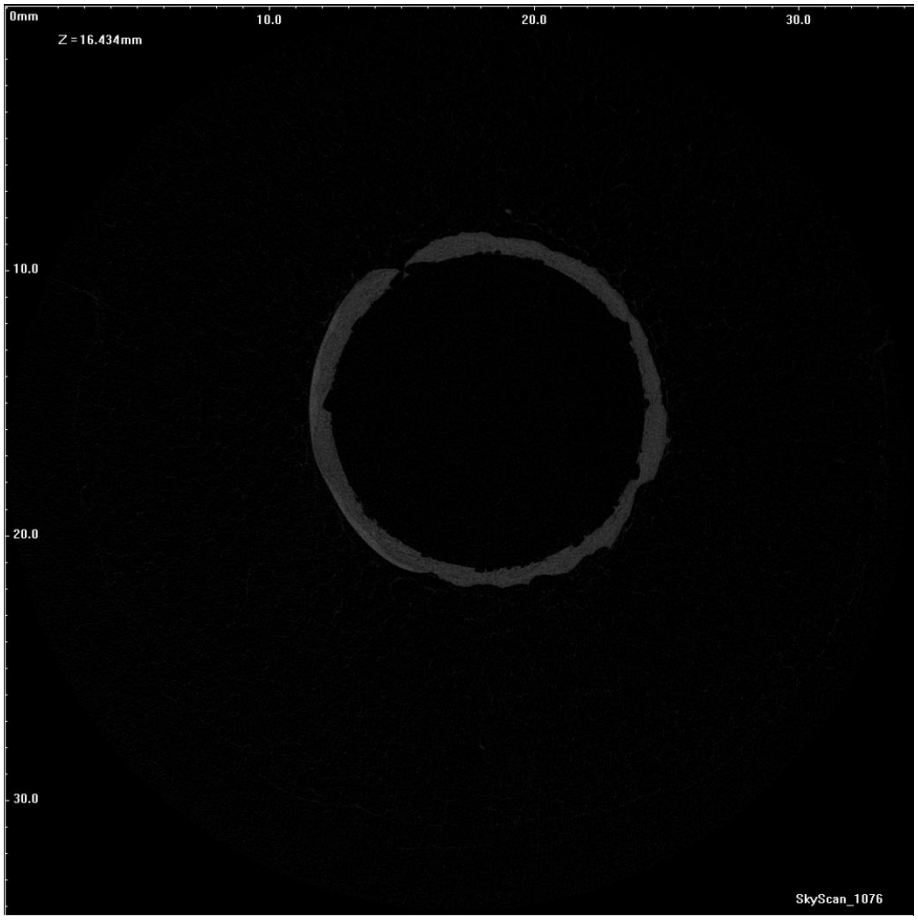

Figure 2: Two-dimensional cross-sectional image slice of a tubular composite braid sample

2.1 Braid Geometry Reconstruction

Reconstruction of the tubular braided composite sample into a 3-dimensional (3D) model was carried out using a 3D image processing software package (ScanIP, SimpleWare, Bradninch Hall, United Kingdom). Bitmap images were resampled by a factor of 50% reduce memory used during the modeling process. Resampling the images reduces memory usage from 636 megabytes to 79 megabytes. A recursive Gaussian smoothing filter of 1 voxel was used to remove grayscale noise and small ring artifacts. A grayscale threshold between 20 and 50 was applied to the images to capture the features of the braid sample in a mask. The mask was inverted and a morphological close of 2-voxel intensity was used. The mask was then re-inverted to remove small islands scattered around the CT images. The final recreated 3D geometry was exported as a stereo lithography (STL) file and then imported into a scientific

visualization package (ParaView, Kitware, Clifton Park, NY). The recreated 3D geometry is shown in Figure 3. The recreated braid geometry shows the undulation of the individual fiber strands as well fiber stand texture.

Figure 3: Three dimensional braid geometry recreated from uCT images

2.2 Void Content and Surface Imperfection Determination

2.2.1 Void and Surface Imperfection Identification

The void content and surface imperfections of the tubular braid sample was examined by determining the volume and distribution of the voids and surface imperfections within the sample. Voids can be seen in the individual 2D image slices of the braid sample (Figure 4). The braid sample in this study exhibited fully enclosed voids which occurred between the inner and outer diameter of the sample (Figure 4). Imperfections caused by the complex undulating architecture of the braid fibers can also be seen in the cross-sectional braid images (Figure 3 and Figure 4). Enclosed voids and surface imperfections will be examined individually.

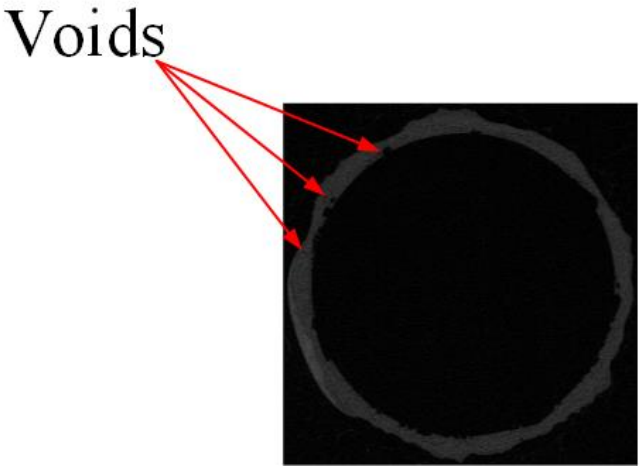

Figure 4: Enclosed voids within the braid sample

Both the enclosed voids and surface imperfections were examined using the same process. To analyze voids and imperfections the braid sample mask created using ScanIP was duplicated to form a second mask identical to the first. A morphological close of 10 voxels was used to close regions where voids were present. A Boolean subtraction of the original braid mask with the morphologically closed mask was used to determine the sample void content. The masking process for examining braid imperfections is illustrated in Figure 5. The volumes of the braid sample mask and the void content mask were determined by calculating the voxel volume of the braid and imperfection masks using the "Volume" command in SimpleWare ScanIP such that void volume fraction could be quantified using equation 1. The braid sample mask was used to compute the braid sample volume (V_{sample}) and the braid void mask was used to determine the sample void volume (V_{voids}).

$$\%V_{voids} = \frac{V_{voids}}{V_{sample} + V_{voids}} \quad \textbf{1}$$

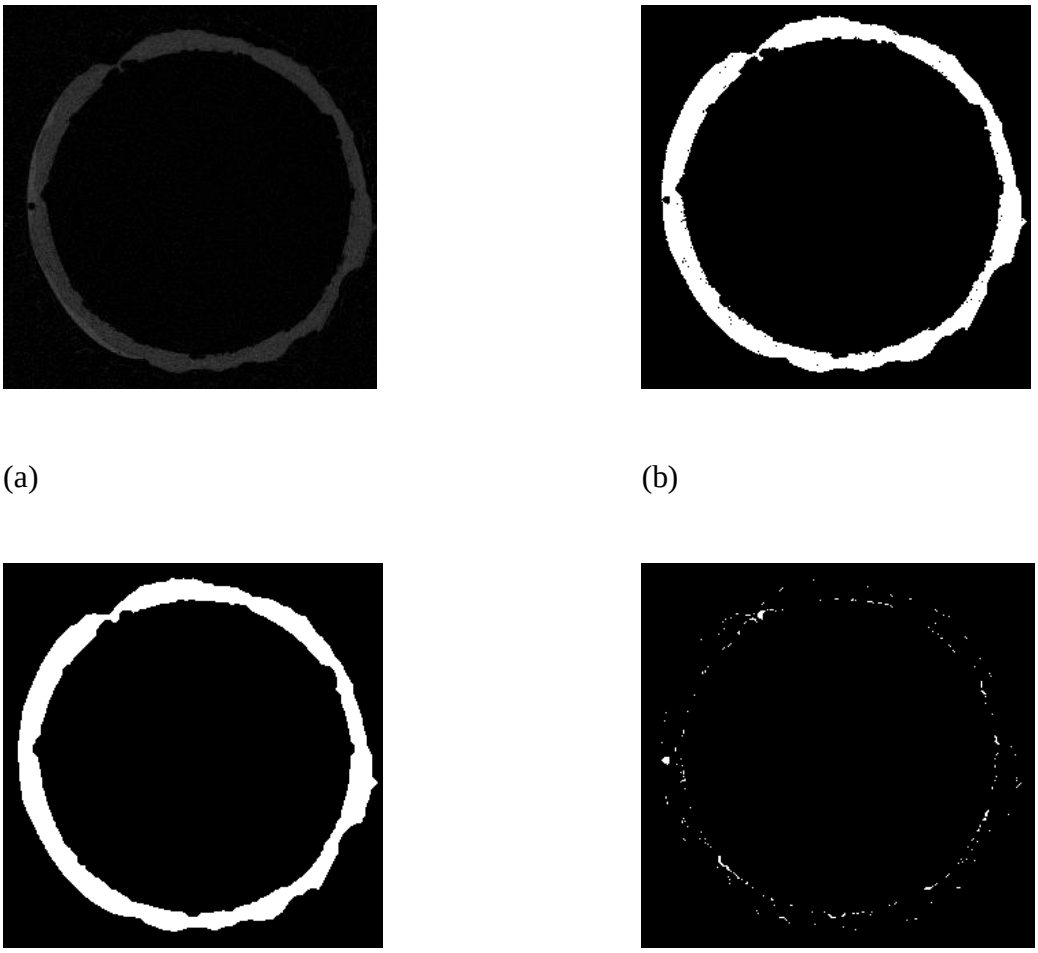

(a) (b)

(c) (d)

Figure 5: Determination of tubular braid void content (a) Initial bitmap image (b) binarized image (c) image and mask overlay to determine braid void content (d) final image of braid surface imperfections

2.2.2 Void Size and Distribution Analysis

Analysis of void size and distribution was performed using a custom image analysis program (MATLAB R2014a, The MathWorks Inc, Natick, MA, USA). The void mask created in Section 2.2 was exported as a RAW image stack and then imported using the custom image analysis program. Void size and distribution was examined by identifying individual voids. Individual

voids were identified by identifying connected regions using the MATLAB function 'bwconncomp'. After identifying each individual void the voxel volume and centroid of each individual void was computed using the command 'regionprops'. Once each void was identified the 3D void geometry was exported to Paraview to visualize the 3D void distribution.

2.3 Tubular Braid Flattening Algorithm

To simplify the analysis of the braid geometry a flattening algorithm was applied to the tubular braid μCT images. Flattening the braid images simplifies the braid strand identification process and allows for automation of the braid strand analysis. In order to view the braids as a flat weave, a transformation of the original circular braid images was performed. Two pieces of information were necessary to perform this transformation, termed "unwrapping": (1) the apparent center of the tubular braid cross section and (2) the radius at which the unwrapping was to occur. If the origin of the braid center was offset, the braid would not appear as flat (*image of incorrectly unwrapped braid)*. If the unwrapping was performed at a radius other than that of the braid yarns, then the pixels in the region of interest (ROI) would be unnecessarily stretched or compressed, adding in extra data (*image of stretched/compressed braid)*.

2.3.1 Location of Braid Origin

As in Figure 2, one plane view of the original μCT scans captured slices of the circular cross-section of the tubular braids. During the scanning process there was potential error in the longitudinal alignment of the tubular braid that resulted in a progressive spatial shift in the image data. For a single image, this could be corrected manually by overlaying a circle approximating the geometry of the braid onto the image. This was accomplished through the user input of a number of points along the outer radius of the circle, from which a best fit approximation of circle is performed [29]. From this, an estimate for the braid origin is determined at either end of

the set of images. A linear interpolation is performed between the top and bottom slices to determine the approximate origin along the sample at each slice location.

Once the braid origin was identified for the image sequence the image unwrapping algorithm was applied. An example of the unwrapping algorithm is shown in Figure 6. Figure 6 (a) shows an example two dimensional image of a circular object which is to be unwrapped. Figure 6 (b) demonstrates the final image after the unwrapping algorithm has been correctly applied. Correct selection of the origin is critical. Figure 6 (c and d) demonstrates the effect the distortion that can occur when the origin is selected incorrectly, with even a single pixel offset (Figure 6 c) having a significant effect on the unwrapped image.

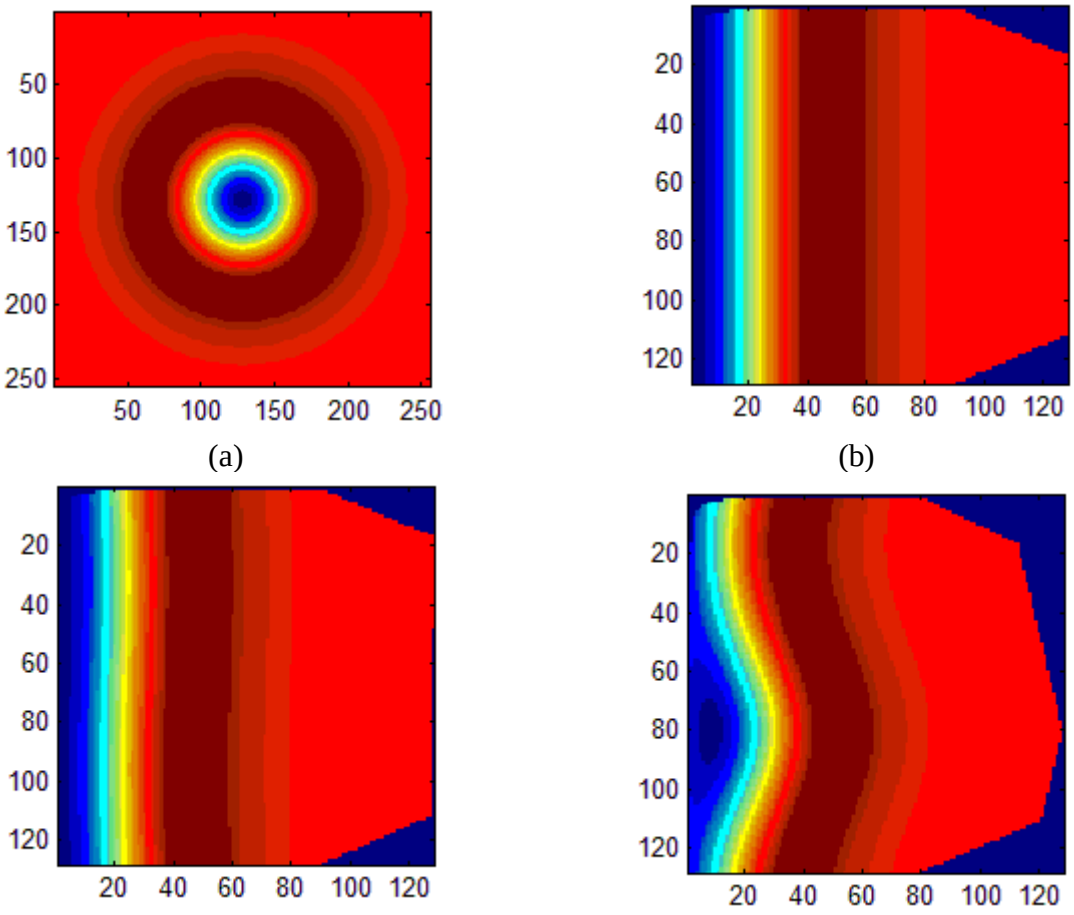

(c) (d)

Figure 6: Example circular image that a unwrapping algorithm is applied to (a) the original image in polar coordinates; (b) image unwrapped correctly with origin located at [128,128]; (c) image unwrapped with slight distortion, origin selected at [128, 129]; and (d) image unwrapped with heavy distortion, origin selected at [120,120]

2.3.2 Determination of Grid Resolution

Mapping an image from polar to Cartesian coordinates will always result in a loss of data [30]. In the images above, the selected grid resolution was 128 by 128 pixels. Both the radial and angular resolutions could be set independently, and selection of these resolutions was critical for an accurate image. At a radius of 10 pixels, there are roughly 63 pixels available to map into the coordinate system. Thus, at a grid resolution of 128 pixels, roughly half of these pixels would have to be interpolated between in order to fill in the data at that location. Above a 20 pixel radius, an interpolation would have to be performed to fill in the data. In an attempt to preserve the accuracy of the data, the dimensional resolution for the image was selected based on the actual circumference and thickness of the tubular braid.

2.4 Braid Strand Analysis

Once the cylinder unwrapping algorithm was applied to the μCT images of a braid sample, the new set of bitmap images were imported into ScanIP. An example of the original and unwrapped bitmap images created using the algorithm described in section 2.3 are shown in Figure 7. The unwrapping algorithm was applied to the braid samples to simplify the segmentation and analysis of the individual yarns within the braid geometry. Similar segmentation techniques as those described above in Section 2.1 were used to form a 3D mask of the unwrapped braid sample. The unwrapped 3D braid geometry is shown in Figure 8.

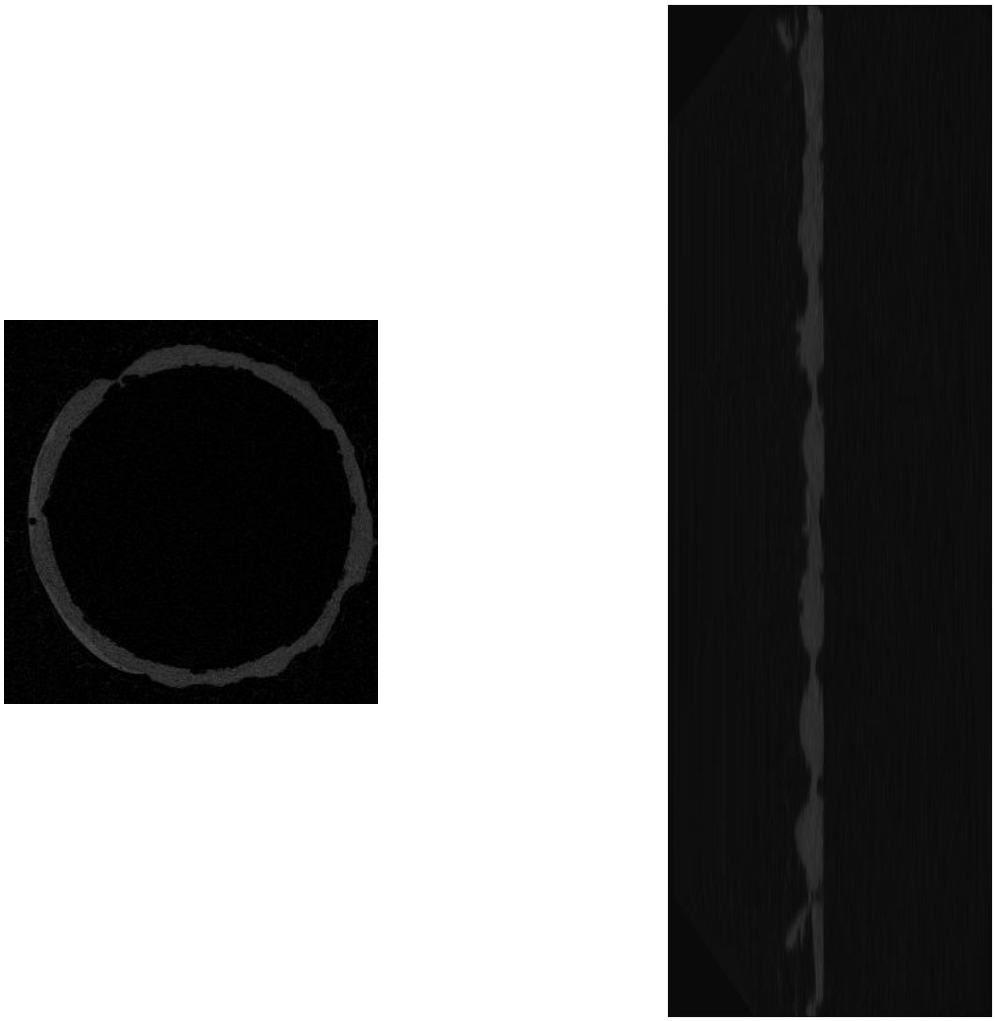

(a) (b)

Figure 7: Braid sample bitmap images (a) original cylindrical braid sample (b) unwrapped braid sample

Figure 8: Unwrapped 3D braid geometry

Once the 3D braid geometry, shown in Figure 8, was created the individual braid strands were segmented. The strands were segmented by using ScanIP's "point to point" line tool in order to identify the individual braid yarns. An example flat braid geometry and strand segmentation lines are shown in Figure 9.

Figure 9: Segmentation of braid yarns

Following braid yarns segmentation, the “3D planar editing tool” in ScanIP was used to bisect the top and bottom halves of the braid sample model, and then capture each half within its own individual mask. As a result of these steps, all strands of the braid sample were separated into several isolated segments. Using a “floodfill” tool the segments of a single strand were captured in a new mask. An example of the final segmented yarn strands is shown in Figure 10.

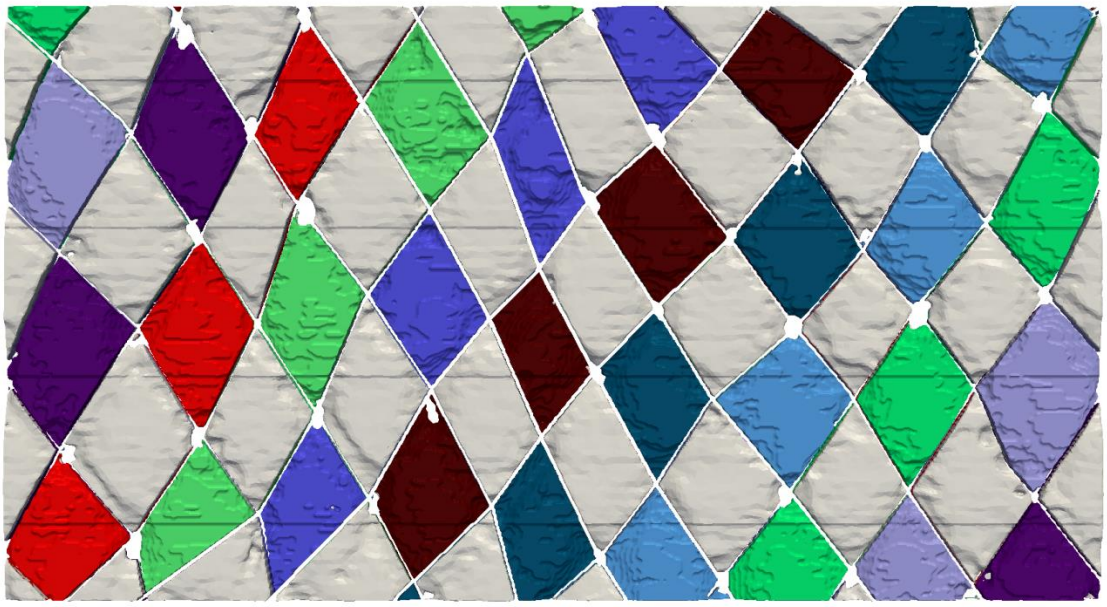

Figure 10: Segmentation of individual braid yarns

Finally, a comparison of the original cylindrical braid geometry and unwrapped braid geometry with segmented yarns is shown in Figure 11. Each of the segmented yarns was assigned an individual grayscale value so that each of the yarns could be analyzed individually.

Figure 11: Unwrapping of original cylindrical µCT scans

A new stack of bitmap images with each yarn identified was created in SimpleWare and then exported. The images were converted to a PNG image stack using and image processing program (ImageJ, National Institutes of Health, Bethesda, Maryland, USA) for further processing. A comparison of an original flat bitmap image and final image with each yarn

identified with a different grayscale value is shown in Figure 12. Figure 12 (b) shows that each braid yarn has been identified with varying grayscale values.

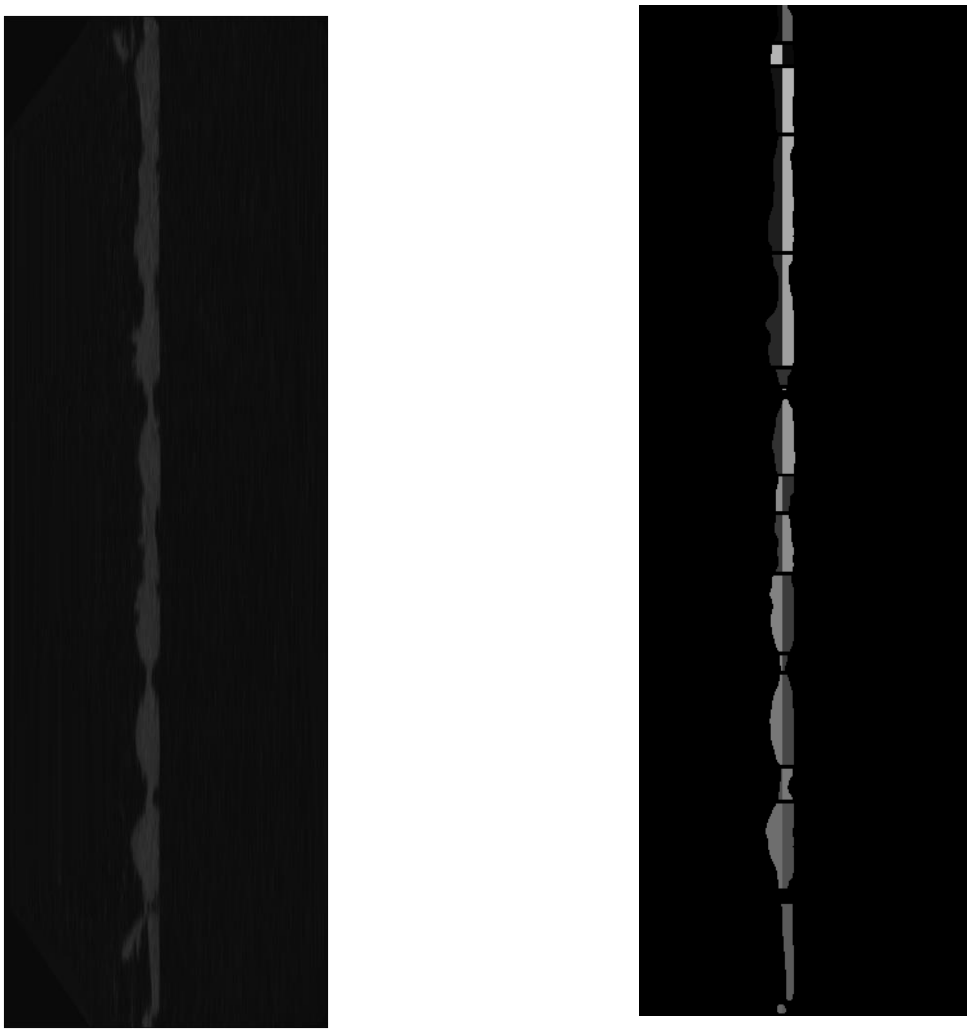

(a) (b)

Figure 12: Identification of individual braid yarns (a) original unwrapped braid image (b) unwrapped braid with a different grayscale value assigned to each yarn

2.4.1 Exportation of Braid Strand Data for Individual Strand Analysis

To quantify the individual braid strand geometries the unwrapped and segmented braid images created in section 2.4 were imported and processed using a custom image analysis program (MATLAB R2014a, The MathWorks Inc, Natick, MA, USA). Here, the centroid, cross-sectional area, aspect ratio, braid angle and fiber undulation period of each strand on each image slice was

determined, with the differing grayscale values of each strand being used to distinguish between each strand.

The position vector, r_{xyz}, describes the instantaneous strand direction. The position vector (r_{xyz}) and the global coordinate system for the flattened braid geometry are shown in Figure 13. The incremental change of a strand's weaving path (crimp angle) was used to track its angular orientation (φ) as it moved along the braid sample by using a rearranged dot product formula:

$$\varphi = \cos^{-1}\left(\frac{r_{xz} \bullet z}{|r||z|}\right) \qquad \mathbf{2}$$

Where r_{xz} is the position vector describing the change of the strand's crimp angle from one image slice to the next in the *x*-*z* plane and *z* is the unit vector in the *z* direction. By similar means, r_{xy}, the incremental change of a strand's braid angle (α) in the *x*-*y* plane, was taken in place of r_{xz} to track the braid angle. Polynomial fits were applied to both the crimp and braid path data to ensure the crimp angle and braid angle data was smooth. A summary of the angle-finding process is shown in Figure 13.

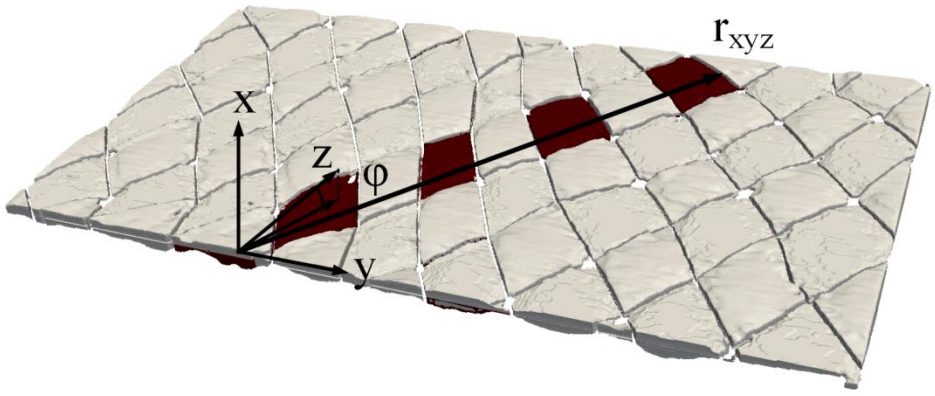

(a)

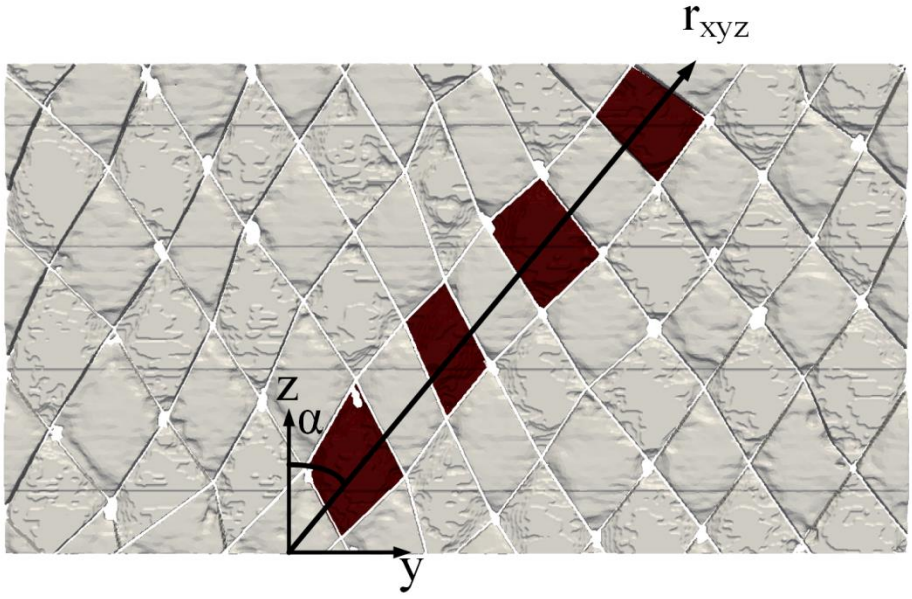

(b)

Figure 13: Summary of angle-finding process: (a) The position vector between centroid coordinates on neighboring image slices, r_{xyz}, describes the instantaneous direction in which a strand moves. Projecting r_{xyz} onto the x-z plane gives a vector describing the strand's instantaneous weaving path, r_{xz}, with the orientation angle being the crimp angle (φ) it makes with the global z axis. (b) Projecting this vector onto the y-z plane gives a vector describing the strand's instantaneous angular path, r_{yz}, with the braid angle (α) being the angle it makes with the global z axis.

Knowledge of the braid angle (α) at all locations along a strand as well as the change in *z* value between each image slice (*dz*) allowed for the global *z* coordinates of the sample to be transformed into local *z'* coordinates for each strand, using the method shown in Figure 13 (b).

At all locations along the braid sample, the cross-sectional area (*A*) of a single strand was found by taking the area recorded from the corresponding image slice, then applying trigonometric correction factors based upon the values of orientation and braid angle found for that strand at the same location along the sample. The orientation angle was used again to correct the maximum height of the strand found for the same image slice. Assuming the cross-section of each strand was elliptical in shape, this allowed the aspect ratio (a_r) of the strand's cross-section to be found at all locations, according to:

$$a_r = \frac{a}{b} = \frac{\pi ab}{\pi b^2} = \frac{A}{\pi b^2} \qquad 3$$

where *a* and *b* are the cross-section's major and minor radii, respectively. Next, the Cartesian coordinates of the CT images were converted to polar coordinates. As the weaving path (*x*-coordinate of the centroid) of the strands was already equivalent to the strand's radial distance from the center of the braid sample, the same value could be used as the polar *r*-coordinate. The θ -coordinate was found using the arc length formula:

$$s = r\theta \qquad 4$$

By treating the full top-to-bottom length of the CT images as the arc length (*s*) when θ was equal to 2π radians, *r* was able to be determined. Then, the θ-coordinate could be found for each strand on each image using:

$$\theta = \frac{y}{r} \quad (5)$$

where y is the y-coordinate of the strand's centroid on a particular image. With the new coordinate system in place, strands could be plotted to reconstruct their tubular structure. The difference in θ coordinates between neighboring parallel strands could be taken to determine the angular spacing between them as they moved along the sample. Using the same tubular datasets, the approximate intersection points between one particular strand and all other strands weaving in the opposite direction could be determined by taking the distance along the z axis at which they were closest together. The intersection points were arranged in order of increasing distance in the global z direction, and then were converted to their equivalent distance along the strand's local coordinate system. Taking the difference in distance between these intersection points, the half-period length (p) of the strand's oscillating weaving path (Figure 14) could be determined at several points along the braid sample.

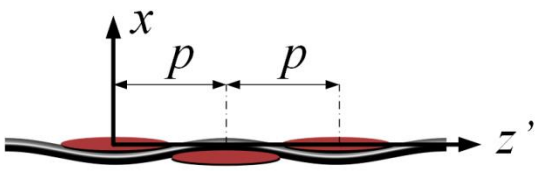

Figure 14: The half period length (p) of the strand's weaving pattern, p, is defined as the length of one half of the strand's (approximately sinusoidal) weaving cycle.

The x-coordinates of all strands at all positions along the braid sample were previously averaged together to quantify the actual radius of the tubular structure. The same was applied to the braid angle, aspect ratio, and cross-sectional area to find their nominal values. Finally, the nominal half period length of the braid sample's strands was determined using:

$$p = \frac{r_0 \beta}{2 \sin \alpha} \quad (6)$$

where β is the shift angle between strands and α is the average braid angle. In all cases, β is simply $2\pi/n$, where n is the number of strands moving in one direction.

All data collected from the strands was plotted as a function of the distance in the z-direction at which it was taken. The oscillating datasets (weaving path, cross-sectional area, aspect ratio, and angular orientation) were plotted with respect to their own local strand coordinates so data for multiple strands could be visualized with minimal phase shift between them. This same data could then be averaged together to view the mean weave path, area, aspect ratio, and angular orientation over the length of a strand.

3 Results

3.1 Void Content and Imperfection Determination

The recreated braid geometry in Figure 3 shows the presence of surface imperfections along the inside diameter of the braid sample. The distribution of imperfection within the braid samples is shown in Figure 15. This figure shows the three dimensional distribution of imperfection throughout the braid sample. Figure 15 (b) and (c) show that many surface imperfections occur along the crossover regions between braid yarns. The section view of the braid sample in Figure 15 (d) illustrates that many imperfections occur along the inside diameter of the sample.

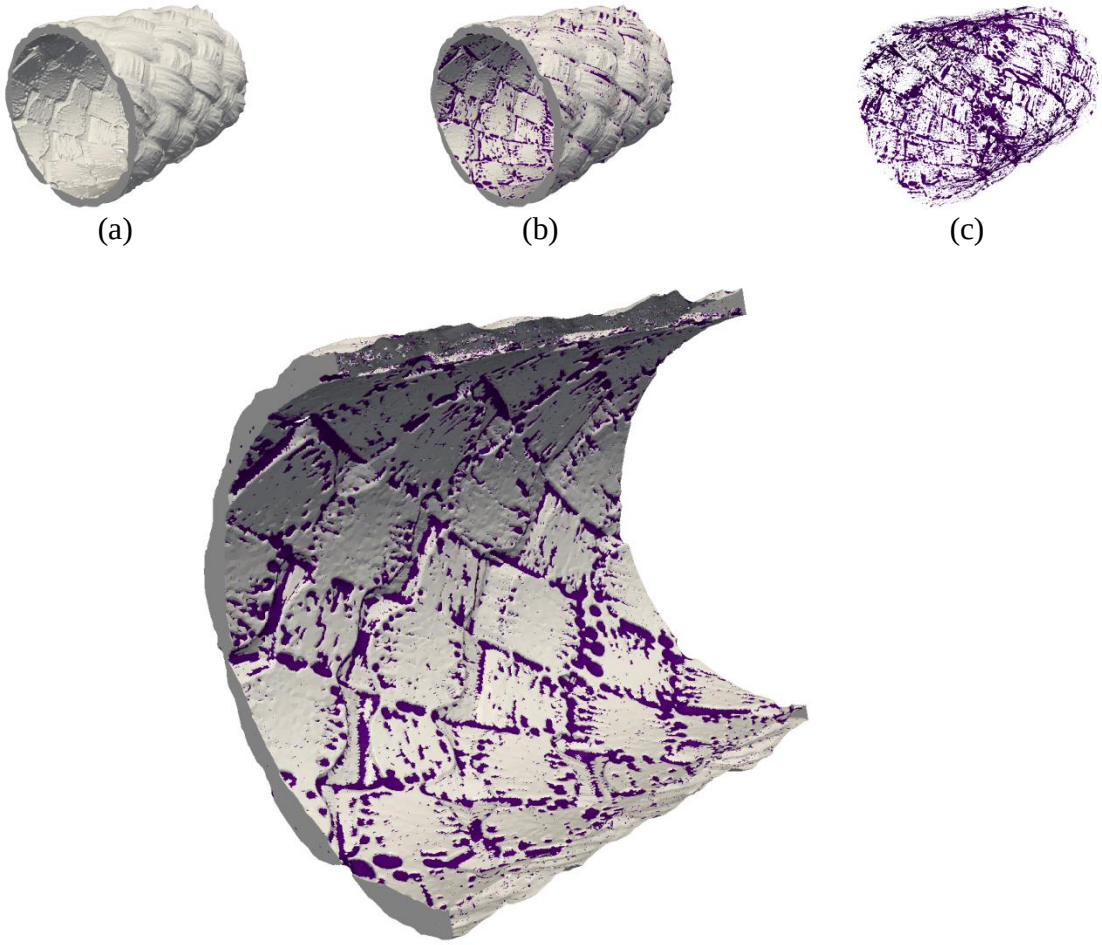

(a) (b) (c)

(d)

Figure 15: Three dimensional visualization of braided composite imperfection distribution (a) 3D braid geometry (b) 3D braid geometry with imperfections (c) 3D dimensional distribution of imperfections throughout the braid sample (d) Cross-sectional view of braid geometry with imperfections

Similarly, the internal enclosed voids were examined and visualized to show the distribution of voids throughout the braid sample. Visualization of the 3D distribution of enclosed voids is shown in Figure 16. Figure 16 (a) shows the entire braid geometry with voids while Figure 16 (b) shows the void distribution. Figure 16 (c) shows a cross-sectional view of the braid sample with enclosed voids.

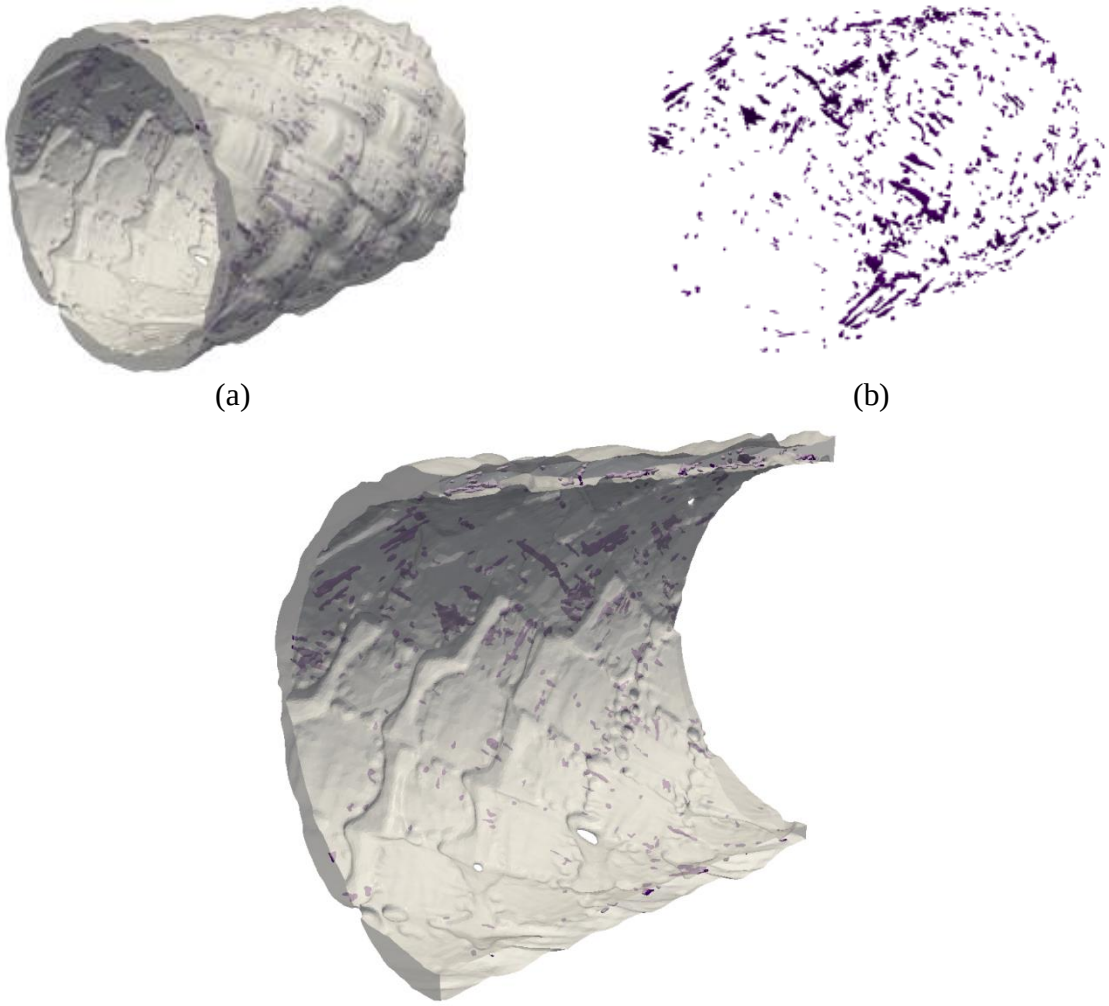

(a) (b)

(c)

Figure 16: Enclosed voids within the braid geometry (a) braid geometry and enclosed voids (b) enclosed voids only (c) section view of braid and enclosed voids

The volume fraction of the imperfections shown in Figure 15 and the voids shown in Figure 16 were determined and are shown in Table 1. The volume of the braid sample as well as the void volume was calculated by determining the voxel volume of the braid geometry, void geometry and imperfection geometry. Table 1 shows that the volume fraction of the braid imperfections is 2.44% while the volume fraction of the enclosed voids was less than half, at 1.04%.

Table 1: Void volume fraction of braid sample

Sample	Sample Volume (mm^3)	Voids Volume (mm^3)	Volume Fraction (%)

Volume fraction of imperfections	424.19	10.61	2.44
Volume fraction of enclosed voids	466	4.91	1.04

3.1.1.1 Void Size and Distribution

Analysis of void size and distribution was performed using a custom image analysis program. Identification of each individual void is shown in Figure 17. In this image, a total of 644 voids were identified. The color map in this image represents the number assigned to each void ranging from 1 to 644.

Figure 17: Identification of individual braid voids

The volume of each void identified in Figure 17 was computed and compared in Figure 18. This figure shows that several large voids are present within the braid geometry having a volume greater than 0.05mm^3 while the majority of the voids have a volume of less than 0.05mm^3. The horizontal line in Figure 18 represents the average void volume. The average void volume for the entire braid geometry was determined to be 0.0076 ± 0.0158mm^3. The largest void within the braid geometry, void # 215 with an area of 0.2248mm^3, can be seen in Figure 18. Figure 19

shows the position of the largest void within the braid geometry. This figure shows the relative size of the largest void to other voids within the braid geometry.

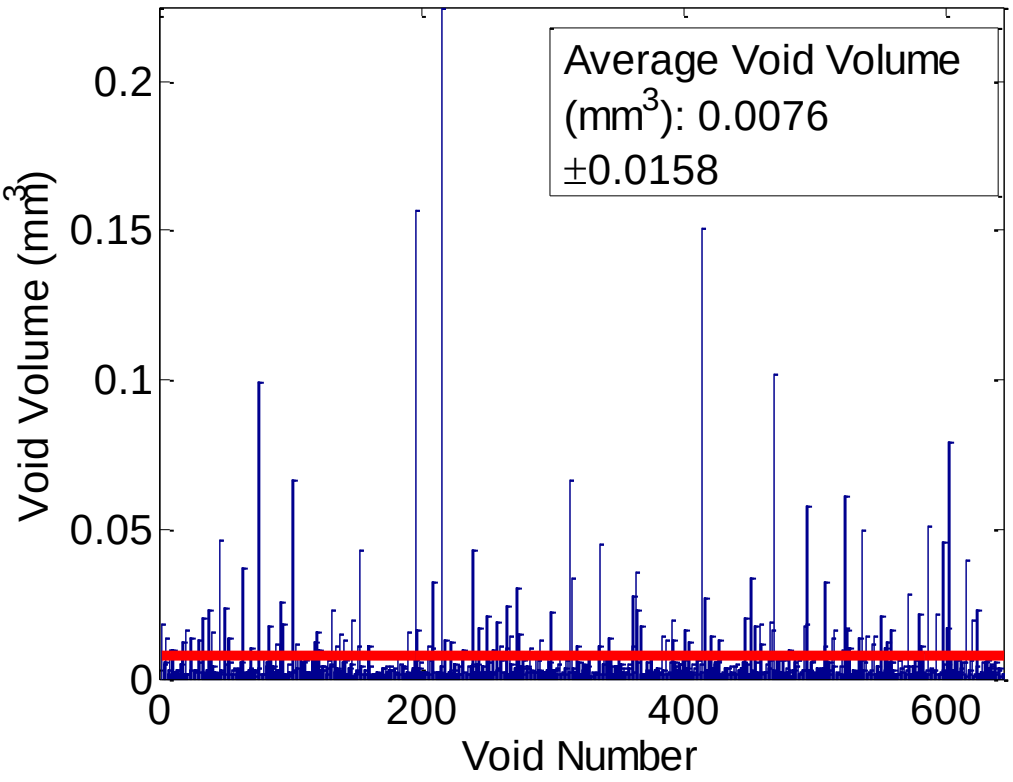

Figure 18: Void volume throughout braid sample. The solid horizontal line indicates the average void volume

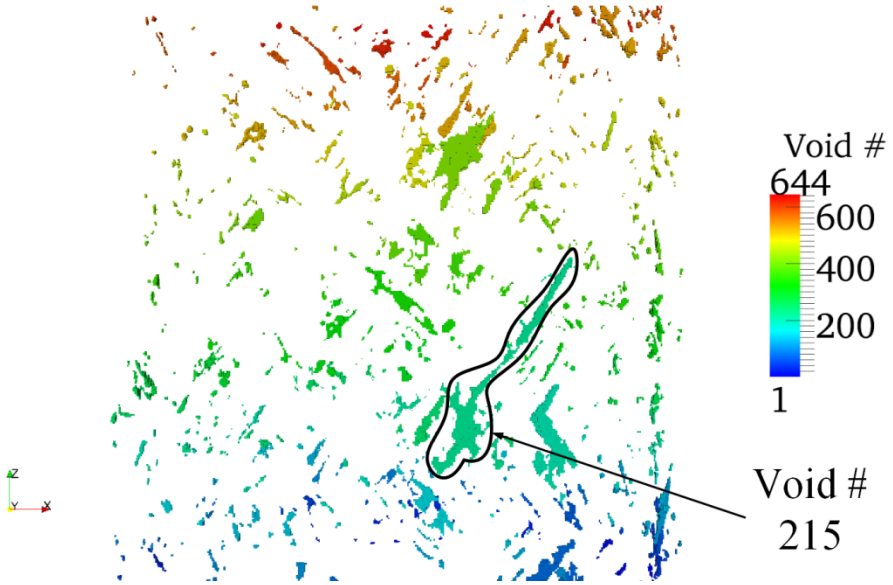

Figure 19: Largest void identified

3.2 Braid Strand Analysis

The unwrapped and segmented braid images were examined using a custom image processing program. The centroid, cross-sectional area, aspect ratio, braid angle and fiber undulation period of each strand was determined, with the differing grayscale values of each strand being used to distinguish between each strand.

The undulating strand path for each of the braid yarns is displayed in Figure 20. This figure shows the weaving path of the individual yarns in the weft and warp directions (Figure 20 (a)). The average weaving path for the braid in both the weft and warp direction is also show in this figure (Figure 20 (b)).

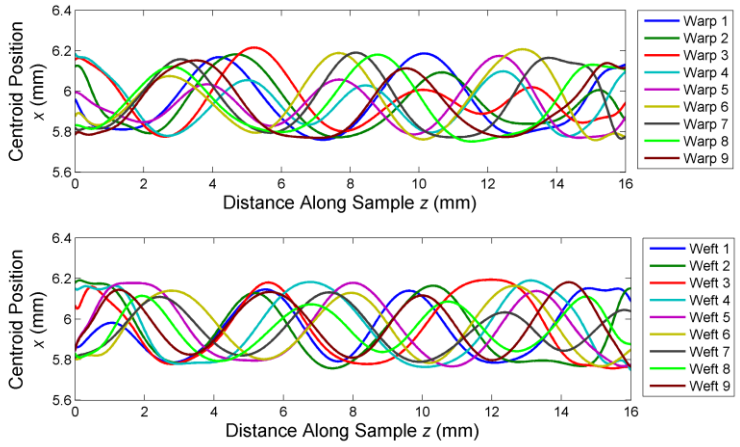

(a)

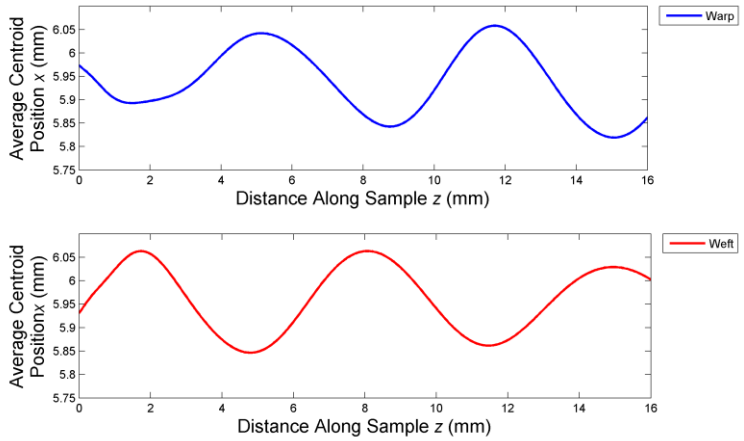

(b)

Figure 20: Weaving path of the braid yarns in the x-z plane (a) weaving path of the individual yarns in the weft (clockwise) and warp (counterclockwise) direction (b) average weaving path of the weft and warp yarns

The angular path of each braid strand in the *y*-*z* plane was also determined. The braid angular path is defined in Figure 13. The angular path of each yarn in both the warp and weft directions is shown in Figure 21.

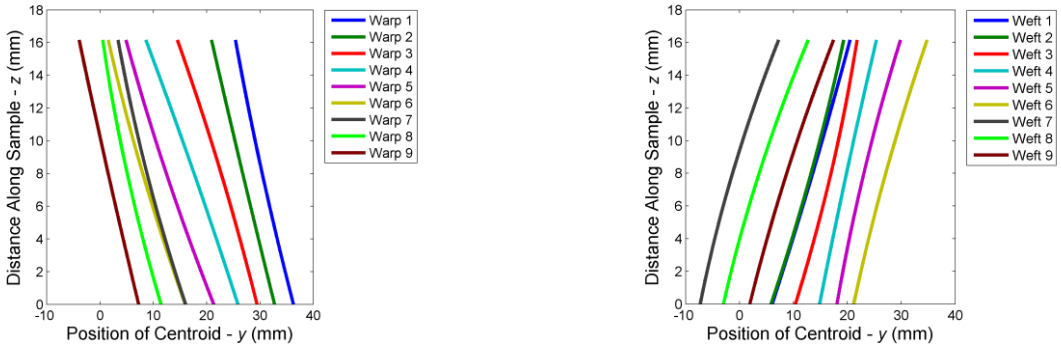

(a) (b)

Figure 21: Angular path of individual braid yarns (a) warp strand angular path (b) weft strand angular path

The results from the braid strand analysis also allowed for the visualization of the 3D path of the yarn centroids. The 3D position of each yarn centroid is visualized in Figure 22. This figure shows the undulating nature of each braid yarn and displays their angular position around the braid circumference.

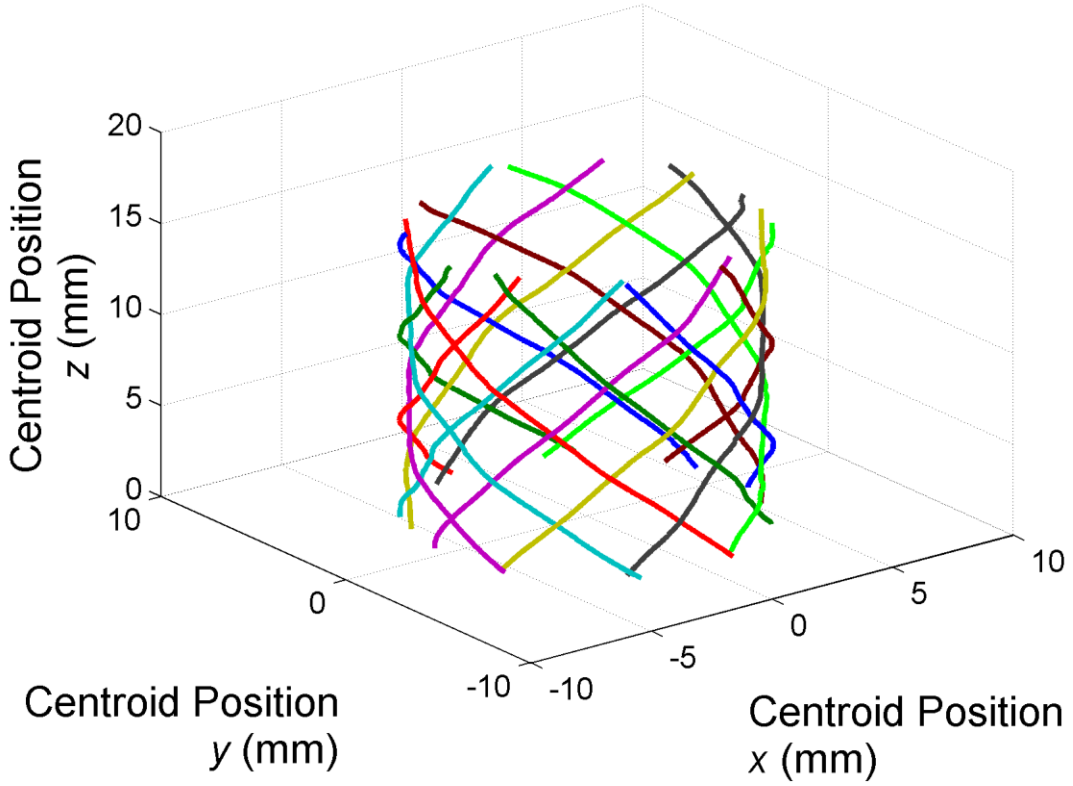

Figure 22: Three dimensional plot of braid centroids determined using the results from the braid strand analysis

The results from the braid strand analysis are shown in Table 2. This table compares the braid strand results for all braid yarns. As well, results are also displayed for yarns in the clockwise (weft) and counterclockwise (warp) directions.

Table 2: Braid strand analysis results comparing all Strands, warp strands and weft Strands of the braid sample with mandrel diameter 11.1 mm

Braid Strand		Radial Distance (mm)	Cross-Sectional Area- A (mm^2)	Aspect Ratio- a_r	Braid Angle –α (deg)	Fiber Undulation Half Period- p (mm)
All Strands	Average	5.95	0.86	7.13	39.26	3.31
	Standard Deviation	0.13	0.14	1.60	5.77	0.49
Warp Strands (CCW)	Average	5.94	0.85	7.25	39.17	3.32
	Standard Deviation	0.13	0.14	1.62	5.76	0.53
Weft Strands	Average	5.96	0.87	7.00	39.35	3.29
	Standard	0.13	0.15	1.59	5.56	0.44

(CW)	Deviation

The weaving paths shown in Figure 20 were used to determine the fiber undulation half period shown in Table 2. The undulation half period of the braid yarns is defined in Figure 14 and equation 6. Figure 20 shows the sinusoidal path of the centroids of the individual braid yarns.

The cross-sectional area and aspect ratio of each yarn shown in Table 2 were determined by assuming the yarns have an elliptical shape [9, 31]. The aspect ratio of each yarn was determined by the cross-sectional area of each yarn from the grayscale images and using equation 3. The angular strand paths in Figure 21 were used to calculate the braid angle (α) of each yarn.

4 Discussion

There are several studies that have utilized the μCT imaging technique in order to investigate composite materials [11, 12, 19-22, 25, 32, 33]. Currently, no studies exist that examine tubular braided composites using the μCT imaging technique. The method outlined in this manuscript will allow for both the investigation of voids within tubular composite braids and evaluation of braid strand geometry. Demonstrating this capability in the complex tubular braid architecture allows this method to be applied to a broad range of composite materials and structures.

4.1 Void Content Determination

Void content has previously been assessed for tubular braided composites using acid digestion and ultrasonic methods however neither of these methods provide information on the statistical distribution of voids throughout a composite sample [26, 27]. Kruesi *et al* found void volume fractions that ranged from 1.74-3.71% for composite braids measured using conventional void volume fraction measurement techniques [26]. The void content in this study was found to be

1.04% for enclosed voids and 2.44% for surface imperfections. Previously, a successive polishing and imaging method has been used to characterize the void distribution of a plain weave textile composite [14]. In this study common void locations and common void shapers for textile composites were identified. However, void volume fraction and void statistics were not reported.

A study by Zhu *et al* examined the effect of void content on the tensile strength of fabric laminates [34]. This study demonstrated that an increase in void content from 0.4% to 8% results in a decrease in longitudinal tensile strength of 2%. It was also demonstrated that crack initiation and growth is caused by the presence of voids within the composite structure. This study demonstrates the importance of minimizing void content since voids result in a reduction in composite material tensile strength. As well, voids within the epoxy matrix initiate crack growth which leads to premature failure of the composite material.

Imperfections and voids can be seen throughout the tubular braid sample examined in this study (Figure 3, Figure 15, Figure 16). The enclosed voids and imperfections were examined separately since these defects are caused by differing mechanisms. The imperfections along the inside diameter of the braid sample shown in Figure 15 are due to the undulations of the braid yarns. The imperfections occur along the cross-over regions between the braid yarns. By contrast, the enclosed voids only occur within the braid geometry as shown in Figure 16. The enclosed voids are caused entrapped air within the resin and braid yarn. The enclosed voids are randomly distributed throughout the braid sample whereas the braid imperfections follow the braid strand path.

The comparison of the volume fractions of the enclosed voids and imperfections is shown in Table 1. This table shows that the imperfection volume fraction is greater than the enclosed void volume fraction. The difference in void and imperfection volumes is also demonstrated in Figure 15 and Figure 16**Error! Reference source not found.**.

The tubular braided composite sample used in this study was manufactured using a manual impregnation process. The above void and imperfection analysis show that defects occurred in the braid sample due to the current resin impregnation process. In order to improve the consistency of resin impregnation and to minimize the number of voids and imperfections in the braid sample a resin transfer molding (RTM) or vacuum assisted resin transfer molding process (VARTM) should be employed [35]. The μCT measurement technique and image processing method outlined in this manuscript can then be used to assess the improved consistency of resin impregnation of various resin impregnation methods.

4.2 Braid Strand Analysis

The μCT measurement technique has allowed for a variety of braid geometrical parameters to be investigated. Similar analysis for flat three-dimensional textile composites has been performed by Bale et al [33]. The results from this analysis provide a wealth of information for braid geometries. Information obtained using this method includes the braid angle of the individual yarns and the radial distance of braid yarns from the braid center. Other parameters that can be determined include: yarn cross-sectional area and aspect ratio and the individual yarn crimp angle. All of the information collected using the μCT measurement technique can be used to assess the quality and consistency for manufactured braids without damaging the braid sample.

The geometrical parameters measured using the μCT measurement technique can be used to compare physical braid geometrics with idealized braid geometry models [9].

Current analytical and finite element models for tubular braided composites utilize idealized geometries in order to predict braid mechanical properties [6, 9, 10, 36, 37]. All of these models make assumptions regarding the braid geometry such as the yarn cross-sectional shape; yarn major and minor diameters; fiber undulation period; as well as, matrix and fiber volume fractions. Key parameters like braid angle have been measured by wrapping transparent paper on the specimens and manually measuring the angle using a protractor [5]. Similarly, assumptions regarding yarn shape and size have been made based on two dimensional micrographs of yarns [31]; however this method does not capture variations in yarn shape and size throughout the braid sample. Therefore, the ability to quantify tubular braid geometry in three dimensions will result in improved tubular braid models since measurements of all braid yarns can be performed.

In addition to improving current models, the three dimensional braid geometry generated in this study could be used for finite element analysis (FEA) [38]. A FEA model generated using the geometry created in this study would allow for examination of the effect of surface imperfections and voids on mechanical properties. The voids and imperfections shown in Figure 15 and Figure 16 will result in stress concentrations that will have a significant effect on braid mechanical properties [34]. This FEA model could also be compared with FEA models created using idealized braid geometries [36] to demonstrate the effect for fiber strand variations and imperfections on mechanical properties.

5 Conclusions

A μCT measurement method has been utilized in order to investigate tubular braided composites. This measurement method has been used to quantify the presence of voids and imperfections in the braid structure. In addition, this method allows for assessment of the three dimensional geometry of composite braids. The method outlined in this manuscript can be used to assess the quality and consistency of the tubular braided composite manufacturing process. Understanding the three dimensional geometry of tubular braided composites will lead to improved analytical models since these models are sensitive to braid geometric effects. In addition, the three dimensional braid geometry generated in the study could also be for further finite element studies.

6 Acknowledgements

The authors would like to acknowledge the support of Natural Sciences and Engineering Research Council of Canada (NSERC).

7 References

References

[1] F. K. Ko, C. M. Pastore and A. A. Head, *Handbook of Industrial Braiding.* Covington, Kentucky: Atkins and Pearce, 1989.

[2] D. Branscomb, D. Beale and R. Broughton, "New directions in braiding," *Journal of Engineered Fibers and Fabrics,* vol. 8, pp. 11-24, 2013.

[3] F. K. Ko, "Braiding," in *ASM International, Engineered Materials Handbook*Anonymous American Society of Metals, 1987, pp. 519-528.

[4] C. Ayranci and J. Carey, "2D braided composites: A review for stiffness critical applications," *Composite Structures,* vol. 85, pp. 43-58, 2008.

[5] C. Ayranci and J. P. Carey, "Predicting the longitudinal elastic modulus of braided tubular composites using a curved unit-cell geometry," *Composites Part B: Engineering,* vol. 41, pp. 229-235, 2010.

[6] J. Carey, M. Munro and A. Fahim, "Longitudinal elastic modulus prediction of a 2-D braided fiber composite," *J Reinf Plast Compos,* vol. 22, pp. 813-831, 2003.

[7] T. Ishikawa and T. -. Chou, "Stiffness and strength behaviour of woven fabric composites," *J. Mater. Sci.*, vol. 17, pp. 3211-3220, 1982.

[8] N. K. Naik and P. S. Shembekar, "Elastic behavior of woven fabric composites: I-lamina analysis," *J. Composite Mater.*, vol. 26, pp. 2196-2225, 1992.

[9] T. Alpyildiz, "3D geometrical modelling of tubular braids," *Text. Res. J.*, vol. 82, pp. 443-453, 2012.

[10] P. Potluri, A. Rawal, M. Rivaldi and I. Porat, "Geometrical modelling and control of a triaxial braiding machine for producing 3D preforms," *Composites Part A: Applied Science and Manufacturing*, vol. 34, pp. 481-492, 2003.

[11] Y. Nishikawa, S. Baba and M. Takahashi, "Optimization of x-ray computerized tomography for polymer materials," *International Journal of Polymeric Materials and Polymeric Biomaterials*, vol. 62, pp. 295-300, 2013.

[12] A. E. Scott, I. Sinclair, S. M. Spearing, M. N. Mavrogordato and W. Hepples, "Influence of voids on damage mechanisms in carbon/epoxy composites determined via high resolution computed tomography," *Composites Sci. Technol.*, vol. 90, pp. 147-153, 2014.

[13] Anonymous "ASTM D2734-09 standard test methods for void content of reinforced plastics," ASTM International, West Conshohocken, PA, 2009.

[14] Y. A. Gowayed, "The Effect of Voids on the Elastic Properties of Textile Reinforced Composites," *J. Composites Technol. Res.*, vol. 19, pp. 168-173, 1997.

[15] I. M. Daniel and O. Ishai, *Engineering Mechanics of Composite Materials*. New York: Oxford University Press, 2006.

[16] F. J. Guild and J. Summerscales, "Microstructural image analysis applied to fibre composite materials: a review," *Composites*, vol. 24, pp. 383-393, 1993.

[17] M. H. Hassan, A. R. Othman and S. Kamaruddin, "Void content determination of fiber reinforced polymers by acid digestion method," *Advanced Materials Research*, vol. 795, pp. 64-68, 2013.

[18] Anonymous "ASTM E1441-11 standard guide for computed tomography (CT) imaging," ASTM International, West Conshohocken, PA, 2011.

[19] L. P. Djukic, I. Herszberg, W. R. Walsh, G. A. Schoeppner, B. Gangadhara Prusty and D. W. Kelly, "Contrast enhancement in visualisation of woven composite tow architecture using a MicroCT Scanner. Part 1: Fabric coating and resin additives," *Composites Part A: Applied Science and Manufacturing*, vol. 40, pp. 553-565, 2009.

[20] L. P. Djukic, I. Herszberg, W. R. Walsh, G. A. Schoeppner and B. Gangadhara Prusty, "Contrast enhancement in visualisation of woven composite architecture using a MicroCT Scanner. Part 2: Tow and preform coatings," *Composites Part A: Applied Science and Manufacturing,* vol. 40, pp. 1870-1879, 2009.

[21] F. Desplentere, S. V. Lomov, D. L. Woerdeman, I. Verpoest, M. Wevers and A. Bogdanovich, "Micro-CT characterization of variability in 3D textile architecture," *Composites Sci. Technol.,* vol. 65, pp. 1920-1930, 2005.

[22] M. Kosek and P. Sejak, "Visualization of voids in actual C/C woven composite structure," in *Special Issue on the 12th European Conference on Composite Materials, ECCM 2006,* 2008, pp. 1465-1469.

[23] J. S. U. Schell, M. Renggli, G. H. van Lenthe, R. Müller and P. Ermanni, "Micro-computed tomography determination of glass fibre reinforced polymer meso-structure," *Composites Sci. Technol.,* vol. 66, pp. 2016-2022, 2006.

[24] J. E. Little, X. Yuan and M. I. Jones, "Characterisation of voids in fibre reinforced composite materials," *NDT and E International,* vol. 46, pp. 122-127, 2012.

[25] P. J. Schilling, B. P. R. Karedla, A. K. Tatiparthi, M. A. Verges and P. D. Herrington, "X-ray computed microtomography of internal damage in fiber reinforced polymer matrix composites," *Composites Sci. Technol.,* vol. 65, pp. 2071-2078, 2005.

[26] A. H. Kruesi and G. H. Hasko, "Computer controlled resin impregnation for fiber composite braiding," in *Int SAMPE Symp Exhib,* 1987, pp. 309-317.

[27] S. D. Senibi, "Application of thermal experimental study to the development of expandable mandrel RTM technique for fabrication of seamless composite tubes," in *International SAMPE Symposium and Exhibition (Proceedings),* 1998, pp. 1310-1321.

[28] Y. Nikishkov, L. Airoldi and A. Makeev, "Measurement of voids in composites by X-ray Computed Tomography," *Composites Sci. Technol.,* vol. 89, pp. 89-97, 2013.

[29] I. Kasa, "A circle fitting procedure and its error analysis," *Instrumentation and Measurement, IEEE Transactions On,* vol. 1001, pp. 8-14, 1976.

[30] W. Park and G. S. Chirikjian, "Interconversion between truncated Cartesian and polar expansions of images," *IEEE Trans. Image Process.,* vol. 16, pp. 1946-1955, Aug, 2007.

[31] J. -. Byun, "The analytical characterization of 2-D braided textile composites," *Composites Sci. Technol.,* vol. 60, pp. 705-716, 2000.

[32] P. Badel, E. V. Sallé, E. Maire and P. Boisse, "Simulation and tomography analysis of textile composite reinforcement deformation at the mesoscopic scale," *International Journal of Material Forming,* vol. 2, pp. 189-192, 2009.

[33] H. Bale, M. Blacklock, M. R. Begley, D. B. Marshall, B. N. Cox and R. O. Ritchie, "Characterizing three-dimensional textile ceramic composites using synchrotron x-ray micro-computed-tomography," *J Am Ceram Soc,* vol. 95, pp. 392-402, 2012.

[34] H. Zhu, B. Wu, D. Li, D. Zhang and Y. Chen, "Influence of Voids on the Tensile Performance of Carbon/epoxy Fabric Laminates," *Journal of Materials Science and Technology,* vol. 27, pp. 69-73, 2011.

[35] P. Potluri, A. Manan, M. Francke and R. J. Day, "Flexural and torsional behaviour of biaxial and triaxial braided composite structures," *Composite Structures,* vol. 75, pp. 377-386, 2006.

[36] L. Xu, S. J. Kim, C. -. Ong and S. K. Ha, "Prediction of material properties of biaxial and triaxial braided textile composites," *J. Composite Mater.,* vol. 46, pp. 2255-2270, 2012.

[37] D. Goyal, X. Tang, J. D. Whitcomb and A. D. Kelkar, "Effect of various parameters on effective engineering properties of 2 × 2 braided composites," *Mechanics of Advanced Materials and Structures,* vol. 12, pp. 113-128, 2005.

[38] P. G. Young, T. B. H. Beresford-West, S. R. L. Coward, B. Notarberardino, B. Walker and A. Abdul-Aziz, "An efficient approach to converting three-dimensional image data into highly accurate computational models," *Philosophical Transactions of the Royal Society A: Mathematical, Physical and Engineering Sciences,* vol. 366, pp. 3155-3173, 2008.